#### **OPEN ACCESS**



# A Millimeter-multiwavelength Continuum Study of VLA 1623 West

Arnaud Michel 6, Sarah I.Sadavo 10, Patrick D.Sheehan Leslie W. Loone 30, and Erin G.Cox 10 <sup>1</sup>Department of Physic⊊ngineering Physics and AstronomQueen's UniversityKingston,ON, K7L 3N6, Canada; arnaud.michel@queensu.ca Center for Interdisciplinary Exploration and Research in Astrono**Nig**rthwestern University1800 Sherman Rd£vanston,IL, 60202,USA Department of AstronomyUniversity of Illinois, Urbana,IL, 61801,USA Received 2022 June 22; revised 2022 August 18; accepted 2022 September 6; published 2022 October 4

#### Abstract

VLA 1623 West is an ambiguous source that has been described as a shocked cloudlet as well as a protostellar disk. We use deep ALMA 1.3 and 0.87 mm observations to constrain its shape and structure to determine its origins better. We use a series of geometric models to fit the uv visibilities at both wavelengths with GALARIO. Although the real visibilities show structures similar to what has been identified as gaps and rings in protoplanetary disks, we find that a modified flat-topped Gaussian modelat high inclination provides the best fit to the observationsThis fit agrees well with expectations for an optically thidkighly inclined disk. Neverthelesswe find that the geometric modelsconsistently yield positive residualsat the four corners of the disk at both wavelengths. We interpret these residuals as evidence that the disk is flared in the millimeter dust. We use a simple toy model for an edge-on flared disk and find thathe residuals bestnatch a disk with flaring that is mainly restricted to the outer disk alR 

30 auThus, VLA 1623W may represent young protostellar disk where the large dust grains have not yet had enough time to settle into the midplane. This result may have implications for how disk evolution and vertical dust settling impact the initial conditions leading to planet formation.

Unified Astronomy Thesaurus concepts: Protostars (1302); Millimeter astronomy (1061); Star formation (1569); Circumstellar disks (235); Young stellar objects (1834)

#### 1. Introduction

young stars. Recent insights from simulations and observations of the outflow cavity wall (Bontemps & Andre 1997; Planets form and evolve in protoplanetary disks around of young disk masses have suggested an early onfisetdust growth leading to planetesimal formation in the Class 0/I protostellar disk phase (Tychoniec at. 2020; Cridland et al. 2022; Drazkowska et al. 2022). Early imprints of this process at a dust continuum polarization observations (Harris et. 2018; work could explain the substructure of two possible rings and gaps attens of astronomicalunits seen in the young Class I protostar, IRS 63 (Segura-Cox etal. 2020). Investigating the morphology of young protostellar disks is therefore necessary to describe the initial conditions and subsequently the dust evolution leading to planet formation.

core within the Oph A region (Pattle et al. 2015) located at distance of ~139 pc (Ortiz-León et al. 2018; Esplin & Luhman 2020). The premier Class 0 source (Andre et al. 1990). VLA 1623 is among the youngest protostars under the voung stellar object(YSO) classification system (Andre et. 1993; Greene et al. 1994; Evans et al. 2009). It has since been!) than its Class 0 companions VLA 1623Aa, Ab, and B identified as a hierarchical system composed of potentially four (Murillo & Lai 2013). The consistent polarization fractions and separate protostars: a very tight protobinary, VLA 1623Aa and morphology from both deep ALMA 1.3 mm (Sadavoy etal. VLA 1623Ab, linked to another companion, VLA 1623B." 1 2 away.as well as VLA 1623 Westlocated ~10/5 west of the triple system (Looney et al. 2000; Murillo et al. 2013; Harris et al. 2018; Kawabe et al2018).

The VLA 1623Aa, Ab binary system has a large energetic outflow (Dent et al. 1995; Yu & Chernin 1997; Caratti o Garatti flux distribution. et al. 2006; Nakamura et al. 2011; White et al. 2015; Hara et al. 10 study VLA 1023VV, we use geometric metal. 2016 sensitive Stokes I continuum ALMA observations at 0.87 and

Original content from this work may be used under the terms of the Creative Commons Attribution 4.0 licence. Any further distribution of this work must maintain attribution to the author(s) and the title of the work, journal citation and DOI.

Lai 2013). In contrast, VLA 1623B and West have been suggested to be shocked cloudlets of leated materialat the Maury et al. 2012; Hara et al. 2021). However, spectral energy distribution analysis (Murillo & Lai 2013), Keplerian rotation (Murillo et al. 2013; Ohashi et al2022c), and high-resolution Sadavoy et al. 2018, 2019) suggest these two sources are disks. This canonical protostellar system thus requires further inquiry to describe the sources in greater detail.

Here, we focus on VLA 1623 West (hereafter, VLA 1623W). Its envelope is low mass ( $\sim$ 0.1  $M_e$ ) and appears more tenuous compared to VLA 1623Aa, Ab (Murillo & The VLA 1623-2417 system is deeply embedded in a dense Lai 2013; Kirk et al. 2017), and it does not display a clear outflow (Nisini et al. 2015; Santangelo et al. 2015; Hara et al. 2021). The proper motion of VLA 1623W is consistent with it co-moving relative to VLA 1623B and fits an ejection scenario from VLA 1623Aa, Ab (Harris et al. 2018), implying a common age. However, it may be a more evolved YSO (Class 2019) and 0.87 mm (Harris et al. 2018) observations are thought to arise from dust self-scattering in a highly inclined optically thick disk implying large ( $\lambda/2\pi \sim 100-300 \mu m$ ) dust grains. As of yet, VLA 1623W has not been modeled and quantitatively described in regards to the millimeter continuum

> 1.3 mm taken from polarization data (Harris et al. 2018; Sadavoy et al. 2019). The models are directly fit to the uv visibilities to constrain the source properties and test if it can be described as a typical protostellar disk. In Section 2, we present the data and simple geometric models used to fit the observed

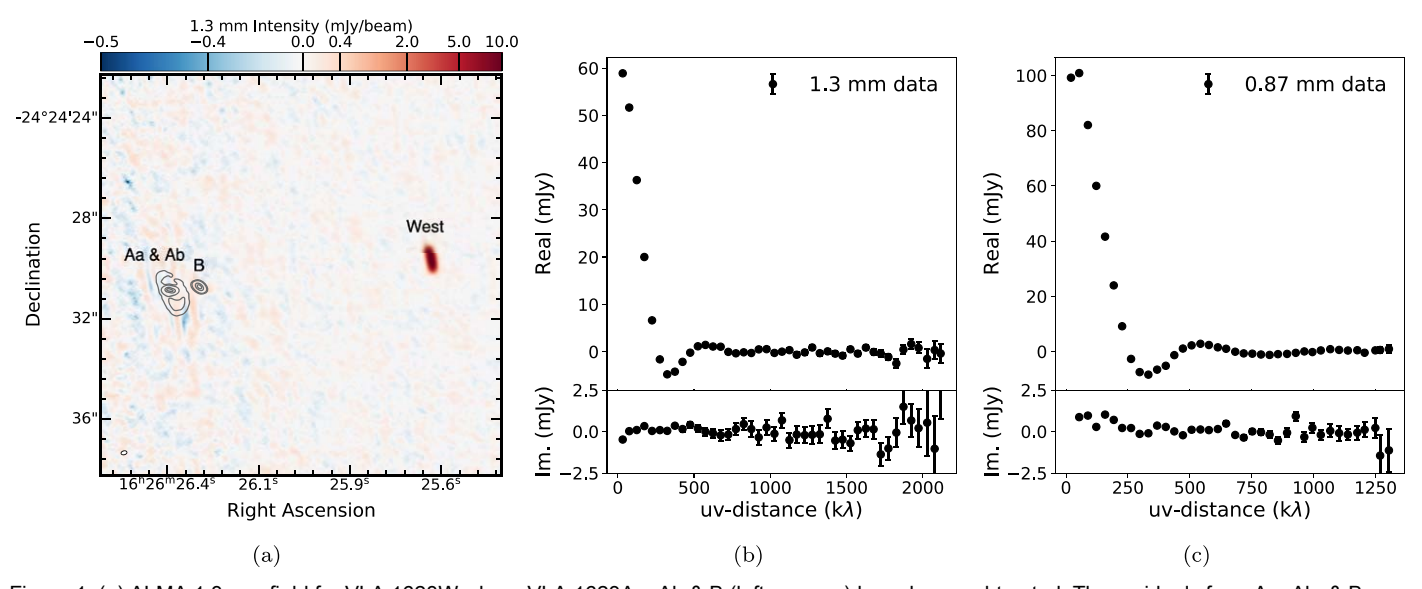


Figure 1. (a) ALMA 1.3 mm field for VLA 1623W where VLA 1623Aa, Ab & B (left sources) have been subtracted. The residuals from Aa, Ab, & B are on the order of 3–5  $\sigma_R$  while the original emission from Aa, Ab & B, shown by the gray contours (20, 50, 100, and 500 braks at 930  $\sigma$ (Aa & Ab) and 980  $\sigma$  (B). On the right, VLA 1623W, is found to peak at 220 (b) ALMA 1.3 mm deprojected and Aa, Ab, B-subtracted uv visibilities centered on VLA 1623W using an inclination of 80°. 3 and a PA of 10°. 3. The uv visibility profiles always display the full data for completeness. At 1.3 mm only the first binned data point is below 50 kλ, locate 40 kλ. (c) Same as panel (b) but for the 0.87 mm data 0.87 mm only the first binned data point is below 50 km hich is located at 20 kλ.

ALMA uv visibilities. In Section 3, we present the results and compare how welldifferent geometric structures mode/LA 1623W. In Section 4. we propose that VLA 1623W is an optically thick flared protostellar disk and discuss the implications of a flared disk and the dangers of misinterpreting substructuresin protostellar disks. Finally, we provide a summary of our findings and avenues for further research in Section 5.

## 2. Methods

#### 2.1. ALMA Observations

VLA 1623W was observed by ALMA polarization projects at 1.3 mm (Band 6), program 2015.1.01112.S (PI: S. Sadavoy), Ine visibilities weights provided by the calibration process have been suggested to be too Looney). The time on source totaled 7.5 minutes in Band 6 with a  $0.27 \times 0.21$  beam (Sadavoy et al. 2019) and 80 minutes in Band 7 with a 0.17 × 0 15 beam (Harris et al. 2018). Both data sets reportpolarization fractions of ~1%-1.5% for VLA 1623W and a uniform polarization aligned with the minor axis. The deep observations required for polarization necessary scaling factor of 0.25 for the visibility weights for which we can detect faint structures (Gulick et aD21).

Both sets of ALMA observations include VLA 1623Aa, Ab, B, and West within the primary beam. While the 1.3 mm observations are centered on West, the 0.87 mm data are centered at an equidistant point between the triple system (Aa, Ab, B) and West. We remove VLA 1623Aa, Ab, and B by modeling these with TCLEAN using Briggs weighting and a robust parameter of 0.5 in CASA 5.2.6.1. The Fourier transform of the TCLEAN modeled emission from VLA 1623Aa, Ab, and B is subtracted from the field using uvsub such that VLA 1623W is the only remaining source of dominant emission; see Figure 1.

To further limit confusion in the visibilities from unrelated extended background emission in the residualsye apply a 50 kλ cut to both data sets. This has been shown to remove (Eisner et al. 2018; Boyden & Eisner 2020). This uv cut corresponds to removing scales \$\square\$550 au and will not significantly impactVLA 1623W itself, which has a compact size of ~100 au (Sadavoy et a2019).

The data above 50 kλ are imaged using robust = 0.5 in CASA. The primary beam corrected sensitivities and the beam sizes for the two wavelengths are  $\sigma_6 = 54 \,\mu\text{Jy}$  beam<sup>1</sup> and  $(0.24 \times 0.15)$  at 1.3 mm (Band 6) and  $\sigma_7 = 110 \,\mu Jv$ beam<sup>1</sup> and  $(0'16 \times 0''15)$  at 0.87 mm (Band 7), respectively. Figure 1 (a) shows VLA 1623W and the successful removal of VLA 1623Aa, Ab, and B at 1.3 mm. The residuals from VLA 1623Aa, Ab, and B are on the order of 3-5 pat 1.3 mm and 3-5 o<sub>7</sub> at 0.87 mm.

large and overconfident, thus requiring rescaling (e.g., Sheehan et al. 2020). Following Sheehan et al(2020) we compare the rms of the naturally weighted TCLEAN image (q<sub>is</sub>) to the uncertainties from the visibility weights (weight of each the visibility), which should follow  $s_{vis} = \sqrt{1/SW_i}$ . We find a detections yield excellent Stokes I continuum sensitivities with both the 1.3 and 0.87 mm data, consistent with the scale factor found by Sheehan et a(2020), i.e., increasing the theoretical noise factor by a factor of 2.

#### 2.2. Geometric Models

We aim to characterize VLA 1623W's disk morphology with the available ALMA observations Figure 1 presents the azimuthally averaged uv visibilities centered on West. The real uv profiles show intensity dips below zero at ~330 kλ and a slight positive enhancement ~550 kλ at both wavelengths. The imaginary (Im) profiles, however, show scatter butlittle obvious structureAs such, we adoptaxisymmetric geometric models to describe the intensity profiles of this source.

Assuming VLA 1623W is a disk, we model it in the visibility plane using a variety of analytic profiles that have some extended emission and improve the disk's rms sensitivitybeen applied to protostellar and protoplanetary disks (see, Tazzari et al. 2021 for a brief list). For simplicity, we focus on models using standard Gaussians and a modified Gaussian with a flat top (FTG). For the standard Gaussian model, we include a additional Gaussian features in the fitting as dips and peaks in real uv visibilities are often indicative of gaps and rings (e.g., Andrews et al. 2021). We use negative Gaussians and positive Gaussians to represent these featurespectively.

We also test a modified FTG model. This model is motivated by the possibility that VLA 1623W as a highly inclined and optically thick protostellar disk, as suggested from polarization observations (Harris et al. 2018; Sadavoy et al. 2019). ALMA millimeter observations of edge-on optically thick disks have found flat brightness profiles along the major axis (Villenave et al. 2020). Furthermore for such sources the disk edge can result in a sharp drop in the millimeter emission (Villenave et al. 2020; Miotello et al. 2022) that cannot be well represented by a regular Gaussian taper. Therefore in the FTG, we use a Gaussian function whose exponent, f is left as free parameter 2 as,

$$I(R) = I_0 \exp\left(-0.5\left(\frac{R}{s}\right)^t\right),\tag{1}$$

where I(R) is the intensity as a function of radius  $R_0$  is the peak intensity at the center, and  $\sigma$  is the standard deviation width. In the case of the standard Gaussian disk and for the ga and ring featureswe fix f = 2.

Lastly, we test a power-law core with an exponentialtail (PLCT) (e.g., Lynden-Bell & Pringle 1974; Andrews et al. 2009; Segura-Cox et al. 2020), which has been used to descri protostellarand protoplanetary disks. The PLCT model can characterize both the disk and the inner envelope components thanks to its two-part surface density structure (Andrews et al. 2009), making it a valuable toolfor protostellar sources with envelope emission traced by millimeter observations. However 1. Fx is the total integrated flux of each function, Gaussian digit, (Gaussian at both wavelengths, the parameter regulating the envelope contribution goes to zero, effectively making a standard Gaussian modelfor VLA 1623W. Therefore we will not discuss the results of the PLCT model further.

For each disk modelye fit the model's free parameters as well as the inclination i of the disk along the line of sight, the position angle PA, and the source offsets from the field center  $\Delta R.A.$  and  $\Delta Dec$  (see Table 1). Note that we fit the total integrated flux (F) as a free parameterrather than the peak surface brightness (1), similar to Sheehan etal. (2020). The parameter space thus ranges from being 6-dimensional (Gaussian disk) to 12-dimension@Gaussian diskgap, ring). We use uniform priors for all parameters see Table 1 for the ranges. We explore the parameter space for the models with a Bayesian approach using an affine-invarian Markov Chain Monte Carlo (MCMC) ensemblesampler, emcee v 2.2.1 (Foreman-Mackey et al. 2013), within the GALARIO python package (Tazzari et a2018).

We generate a 5" radial grid with a 150 arcsecond cell size for which the geometric modelis evaluated. GALARIO then allows us to Fourier transform the 2D geometric models to synthetic visibilities using the baseline pairs from the model on the same scale as the true observations. We minimizet 1.3 mm and in 35 kλ bins at 0.87 mm. Each row of panels the  $\chi^2$  value between the sum of the observed realand Im visibilities compared to the synthetic equivalento find the optimal fit parametersusing 60 walkers over 5000 steps distributed using MPIPool. We image the residuals in CASA,

Table 1 **Disk Profiles** 

Rest-fit Parameters

•	Best-tit Parameters			Prior	
າ Profile	λ	1.3 mm	0.87 mm		
reGaussian Disk od	$F_D \ (mJy)$ $\sigma_D \ (mas)$ $Maximum$ $residuals$	66 <sup>+</sup> 6 300 <sup>+</sup> 1 23.4 <b>q</b> <sub>6</sub>	117 <sup>+</sup> <sup>1</sup> 317 <sup>+</sup> <sup>1</sup> 23.4 σ <sub>7</sub>	$- 4 \log_{10} F_D < 0$ $10 < \sigma_D < 2000$	
Gaussian Disk Gap	$\begin{split} &F_D \text{ (mJy)} \\ &\sigma_D \text{ (mas)} \\ &F_G \text{ (mJy)} \\ &\sigma_G \text{ (mas)} \\ &\text{loc}_G \text{ (mas)} \\ &\text{Maximum} \\ &\text{residuals} \end{split}$	161 16 215 3 - 97 18 150 5 61 6 7.2 G	325 <sup>+</sup> 18 222 <sup>+</sup> 7 - 214 <sup>+</sup> 27 169 <sup>+</sup> 2 146 <sup>+</sup> 1 46 <sup>+</sup> 2 13.4 $\sigma_7$	$- 4  \log_{10} F_D < 0$ $10 < \sigma_D < 2000$ $- 4  \log_{10} F_G < - 1$ $1 < \sigma_G < 500$ $10 < \log_G < 200$	
≨aussian Disk Gap Ring	$\begin{split} F_D & (\text{mJy}) \\ \sigma_D & (\text{mas}) \\ F_G & (\text{mJy}) \\ \sigma_G & (\text{mas}) \\ loc_G & (\text{mas}) \\ F_R & (\text{mJy}) \\ \sigma_R & (\text{mas}) \\ loc_R & (\text{mas}) \\ Maximum \\ residuals \end{split}$	60 <sup>+</sup> 6 274 <sup>+</sup> 1 - 22 <sup>+</sup> 6 238 <sup>+</sup> 19 238 <sup>+</sup> 52 139 <sup>+</sup> 50 25 <sup>+</sup> 2 97 <sup>+</sup> 8 359 <sup>+</sup> 6 6.5 $\sigma_6$	106 <sup>+</sup> 1 274 <sup>+</sup> 1 - 4 <sup>+</sup> 7 2 <sup>+</sup> 1 158 <sup>+</sup> 1 10 <sup>+</sup> 3 2 <sup>+</sup> 1 432 <sup>+</sup> 1 11.6 σ <sub>7</sub>	$-4  \log_{10}F_D < 0$ $10 < \sigma_D < 2000$ $-4  \log_{10}F_G < -1$ $1 < \sigma_G < 500$ $10 < \log_G < 200$ $-4  \log_{10}F_R < -1$ $1 < \sigma_R < 500$ $200 < \log_R < 500$	
FTG ibe s	F <sub>D</sub> (mJy) σ <sub>D</sub> (mas) f Maximum residuals	63 <sup>+</sup> 1 449 <sup>+</sup> 1 5.01 <sup>+</sup> 0.07 5.8 $\sigma_6$	110 <sup>+</sup> 1 459 <sup>+</sup> 1 4.95 <sup>+</sup> 0.03 13.3 0 <sub>7</sub>	$- 4  \log_{10} F_D < 0$ $10 < \sigma_D < 2000$ $2 < f < 10$	

- gap (F<sub>G</sub>), and Gaussian ring (A).
- 2. The Gaussian substructures ps, and rings are offset from the center by a
- 3. Maximum residuals are positive excess emissionall cases, the positive residuals are greater than the negative ones. The residuals are obtained from the cleaned image of the observed visibilities minus the best-fit model visibilities.
- 4. At 0.87 mm for the Gaussian diskgap, and ring model, the value of  $\sigma_G$ appears bimodabver multiple runs, either converging to  $\sigma_G = 2$  mas (with  $loc_G \approx 150$  mas) or  $\sigma_G = 1.0$  mas ( $loc_G \approx 53$  mas). The BIC condition (see Section 3.2) strongly favors the first solution, so we only consider those parameter further. The remaining parameters are consistent between both cases.

which we obtain by subtracting the Fouriertransform of the disk models from the observations in GALARIQo examine the quality of the fit in the image plane.

#### 3. Results and Analysis

## 3.1. Model Fitting Results

Figure 2 shows the best-fit model uv profiles compared to the observationsthereby generating synthetic observations of the 1.3 and 0.87 mm uv data. The uv data are shown in 55 kλ bins displays a different geometric modelfit to the data sets and includes a zoomed-in section of the region where the real data are structured. The geometric models are plotted using the best-fit parametersound in Table 1; these are the median

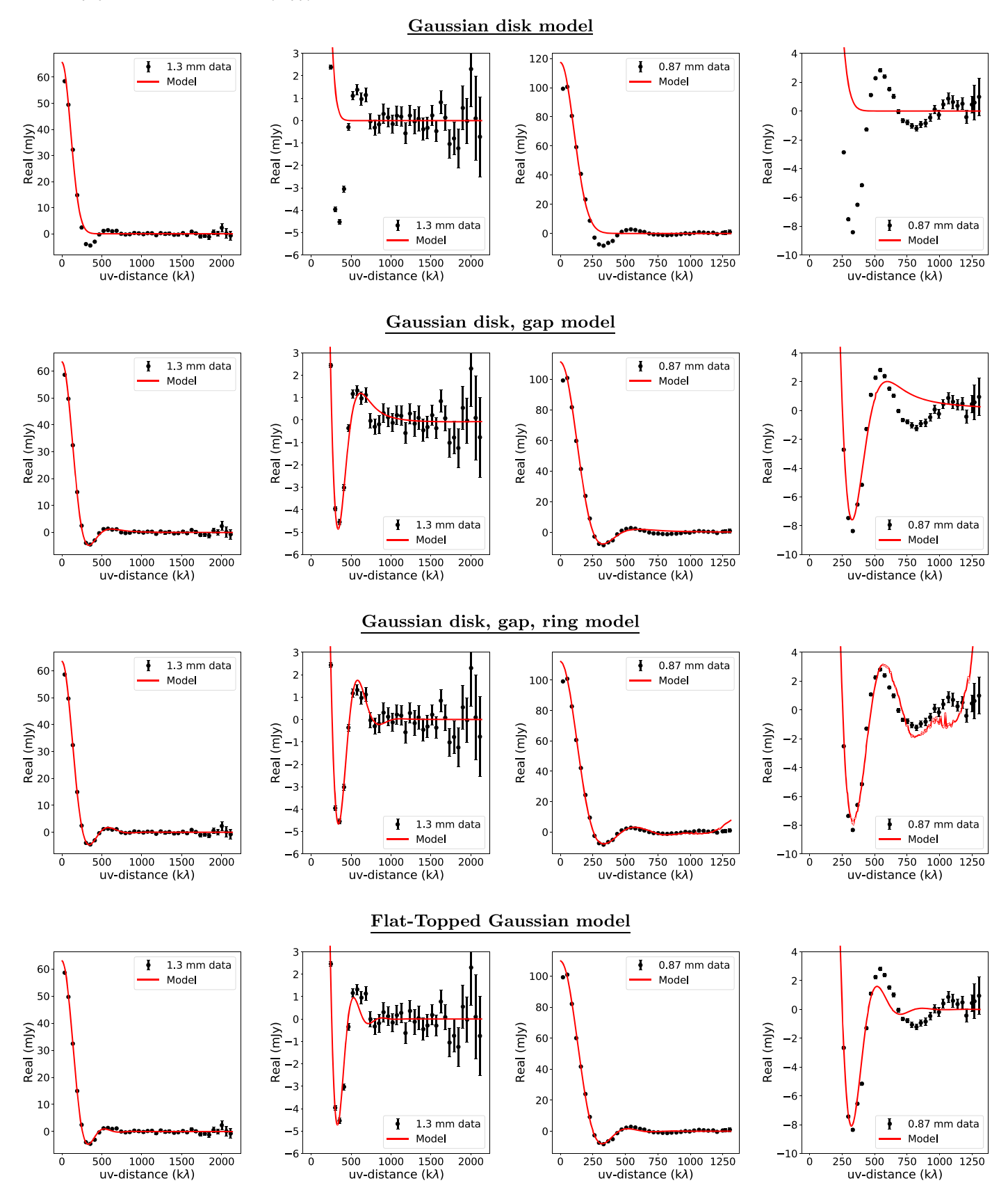
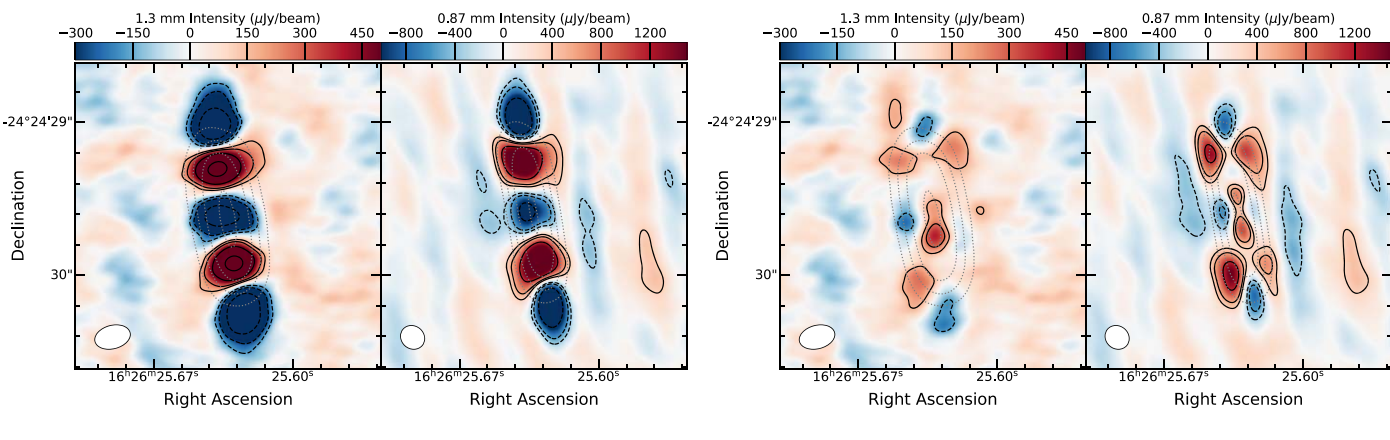


Figure 2. Real uv visibility profiles in black data points fit by a series of different disk models, described in Section 2.2, shown by the red lines; see Table 1 for the best-fit parameters shown her the first left column shows the full 1.3 mm data while the second column shows a zoom in to highlighte region of structured visibilities. The third and fourth columns display the same information for the 0.87 mm observations. The topmost row shows the standard Gaussian disk model, the second row shows the Gaussian display model, the third row shows the Gaussiandisk, gap, ring model, and the fourth and final row shows the FTG model.

#### Gaussian disk residuals

#### Gaussian disk, gap residuals



### Gaussian disk, gap, ring residuals

#### Flat-Topped Gaussian residuals

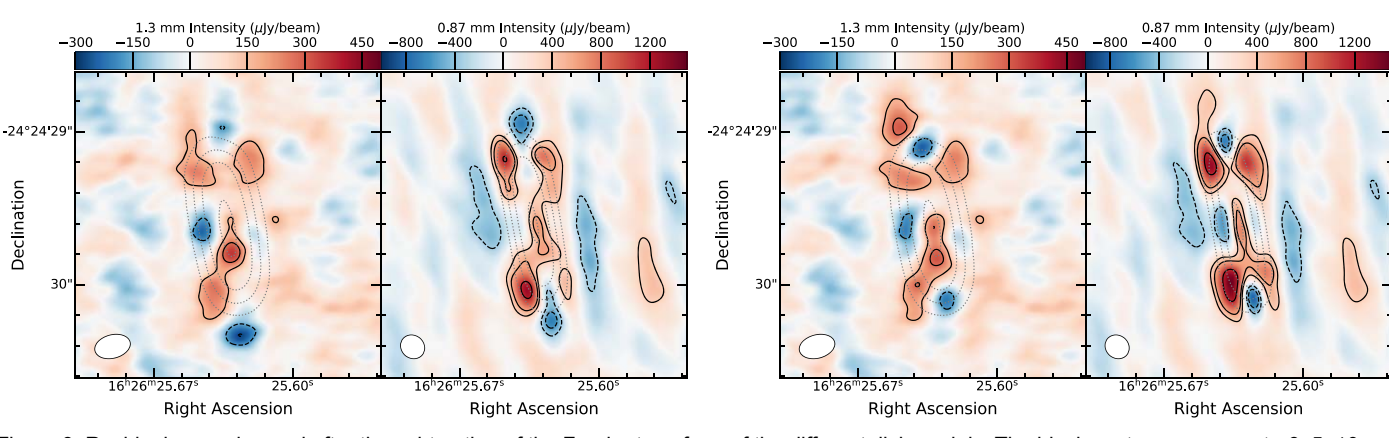


Figure 3. Residuals were imaged after the subtraction of the Fourier transform of the different disk models. The black contours represent ±3, 5, 10, and 20σ residu The gray dotted lines represent e original disk emission at 20, 50, 100, and 200o. In each pair of panels, the left panel represents the 1.3 mm residuals with σ<sub>6</sub> = 54 μJy, and the right panel shows the 0.87 mm residuals with1d0 μJy. Aside from the Gaussian disk model, the three other model residuals are remarkably consistent and similaalbeit with small differencesand generally display positive residuals at the disk's four corners.

values of their posterior distributions with the uncertainties representing the 68% inclusion intervalin general, the disk models unanimously find the same center point the source: R.A. =  $16^{\text{h}} 26^{\text{m}} 25.6315$  and Decl. =  $-24^{\circ}24.29.6184$  at 1.3 mm, R.A. =  $1626^{\text{m}} 25.6315$  and Decl. = -24.2429 5866at 0.87 mm, with PA (10°.3 ± 0°.1), and high inclination  $(80^{\circ}. 3 \pm 0^{\circ}. 1)$  on firming previous results (e.g., Harris et al. 2018; Sadavoy et al. 2019).

Figure 3 shows the imaged residuals from each best-fit model using the same imaging procedure as described in Section 2.1. The residuals are evaluated by subtracting the model's synthetic visibilities from the observations. Figure 3 is thus useful to compare the impact each model has in the image plane, leaving residuals of varying distribution, morphology, and significance. Excluding the standard Gaussian disk case (upper left panel in Figure 3), the other three models show similar positive residuals athe four corners of the disk, with the residuals more pronounced at the north and south corners and BIC both address the quality of the total also the profile the eastern side of the disk compared to the western side. The mplexity. They penalize, albeit differently, the increasing are also negative residuals at the north and south ends along thember of free parametersThe AIC is defined as AIC = disk's major axis. These residuals imply thathere is excess emission off the disk midplane, such that the disk could be geometrically thick or flared (see Section 3.3).

visibilities. The residuals include both significant positive and

negative artifactsup to 23¢ and 23¢. We thus focus on the other geometric models to address these features. The Gaussian disk, gap and Gaussian diskgap, ring models fit the real uv data better and decrease the residuals to  $\sim 76$  and  $\sim 12$   $\sigma_7$ . The FTG uv visibilities and residuals are largely comparable to those of the structured disk models. In this case, the FTG has a sharper disk edge that produces ringing similar to what is seen in the uv visibilities. Since VLA 1623W has an ~80° inclination, we are primarily observing the disk edge-on and as such the dips and peaks in the realisibilities may not be due to disk structures like gaps or rings.

## 3.2. Model Quality

We use statistical tests including the reducedtine Akaike information criterion (AIC; Akaike 1974), and the Bayesian Information Criterion (BIC; Schwarz 1978), to compare qualitatively the models described in Section 3.1. The AIC  $2k + n \ln(RSS/n)$ , where k is the number of free parameters, n the number of data points, and RSS is the residual sum of squares. The BIC is evaluated as BIC =  $k \ln(n) +$ The standard Gaussian disk model does not match the real  $\mathfrak{M}$ n(RSSn). The inclusion of extra parameters inflicts a more severe penalization for the BIC compared to the AIC. Evaluating

Table 2 **Disk Profiles** 

Best-fit Statistics			
1.3 mm	0.87 mm		
5.45	11.54		
-1462	-5463		
-1452	-5452		
5.30	11.42		
-15	-289		
-33	-312		
5.30	11.41		
-20	96		
-64	40		
5.30	11.41		
87612	1208236		
87665	1208315		
	1.3 mm  5.45 -1462 -1452  5.30 -15 -33  5.30 -20 -64  5.30 87612		

Note. AIC<sub>0</sub> and BIC<sub>0</sub> are the reference values from the FTG modesed to compare with the other models. These are relative comparisons between pairsacross the disk models and both wavelengths suggesteal of models and can thus be applied to any pairto compare which modelis superior.

 $\triangle$ AIC and  $\triangle$ BIC between models (i.e.,  $\triangle$ AIC = AIG-AIC<sub>1</sub>) provides a qualitative comparison. Kass & Raftery (1995) model with a lower BIC value, 20 < ΔBIC < 150 as strong evidence, and >150 as decisive evidence. We use the same comparison scale for ΔAIC.

Table 2 shows the results from the statistical tests. We benchmark ΔAIC and ΔBIC against the FTG where the references are AIC = 87,612 and BIC<sub>0</sub> = 87,665 at 1.3 mm and AIC<sub>0</sub> = 1,208,236 and BIC<sub>0</sub> = 1,208,315 at 0.87 mm. Unsurprisingly, we find that the Gaussian disk modelloes a significantly poor job fitting the observations based on the AIC and BIC parameters compared to the FTG. The Gaussian disk, gap modelis also strongly disfavored based on both the AIC and BIC metrics. The Gaussian disk, gap, ring model, however, cannot be fully ruled out as there is strong evidence in favor of it at 0.87 mm.

Nevertheless the Gaussian disk, gap, ring model is not favored at 1.3 mm and the resulting best-fit profile is unlikely to the flaring power, and hoff is added to account for both the be observed with the resolution of the 0.87 mm observations. The best-fitring and gap have widths of order ~0.3 au (~2 mas) which is 75 times lower than the beam resolution. Figure 4 compares the best-fiteometric models studied here both plotted as brightness as a function of radius (top panel) and real visibilities as a function of uv-distance. These two panels highlight the extreme conditions for the Gaussian disk, gap, ring model compared to the other, more smooth, profiles. FTG model using GALARIO to simulate our observations and Such sharp features would be surprising compared to the disks (Segura-Cox et al. 2020; Sheehan et al. 2020). We suggest that this fit deviates from observable solutions to addressing purely the features found in the real uv visibilities. Furthermore, the 1.3 and 0.87 mm structured disk fits are drastically different. In contrast, the FTG is statistically favored (top) and the corresponding imaged residual (bottom); see in nearly every comparison the best-fits are consistent at both wavelengths and it is also the simplestmodel that addresses the observed data as well as our expectation of a highly inclined, optically thick protostellar disk.

We compare the VLA 1623W observations and best-fit models in uv visibility space since the beam-convolved images are very similar due to the large beam size relative to the typical disk structure sizes identified by the best-fit models in Table 1 (see Appendix A1 for more details). Since the uv visibilities are not convolved with the beam, the differences in the models are detectable and we can use statistical tests to distinguish between them.

Regardless of the model, four symmetric positive residual features are generally found at the edges of the disk consistently acrossboth wavelengths; see Figure 3. These residuals vary in their significance depending on the model that is subtracted from the observations but remain similar in their morphology and distribution. These residuals suggest there are features of the disk that are not captured by our simple geometric models and assumptions.

#### 3.3. Toy Model

The symmetry, location, and consistency of the residuals feature of the disk. Given the high inclination of VLA 1623W (~80°), the residuals may be evidence of the outer disk vertical scale height. For young disks the outer edge may still be puffed up (e.g., IRAS 04302; Villenave et al. 2020), because the millimeter-sized dust has yet to settle. The large dust is quantifies 3 < \Delta BIC < 20 to be positive evidence in favor of the expected to settle eventually onto the thircold midplane as observed in more evolved edge-on Class II protoplanetary disks (Villenave et al. 2020, 2022).

Since GALARIO is limited to 2D modeling (Tazzariet al. 2018), we build a simple completely edge-on (90 ared disk toy model based on the best-fit FTG model at 0.87 mm. Briefly, we assume thathe disk scale height(seen as a width when edge-on) increases as a function of radius. The key parameters used to describe the toy model are encapsulated in the vertical disk scale height parameterization that is  $\sigma_h$  of a Gaussian function such that,

$$s_h(R) = h_0 \left(\frac{R}{R_0}\right)^b + h_{\text{off}}, \qquad (2)$$

where  $h_0$  is the height scaling factor,  $R_0$  is the radial scaling factor dictating atwhich radii flaring becomes importanß is geometric thickness of the disk (e.g., it is not necessarily razorthin like Oph163131; Villenave et al. 2022) as well as thickness in the disk from notbeing truly at 90° inclination. We inject random Gaussian noise to match the sensitivity of the observationsclosely. Further details about the toy model's description can be found in Appendix A2.

We take a grid of toy models and fit them with an edge-on then image the residuals of the toy moderninus the best-fit, properties of gaps and rings seen in other Class 0/I protostellar edge-on FTG model. The residuals in this case should represent the remaining emission that's offset from the disk midplane that is not capture by the flat, edge-on FTG model. Therefore, a good toy model should reproduce the observed residual features seen in Figure 3. Figure 5 shows a sample disk model Appendix A2 for additional tests.

> With the edge-on flared protostellar disk toy model, we can reproduce a similar residual morphology at the four corners of the disk. However, we emphasize we are not fitting the

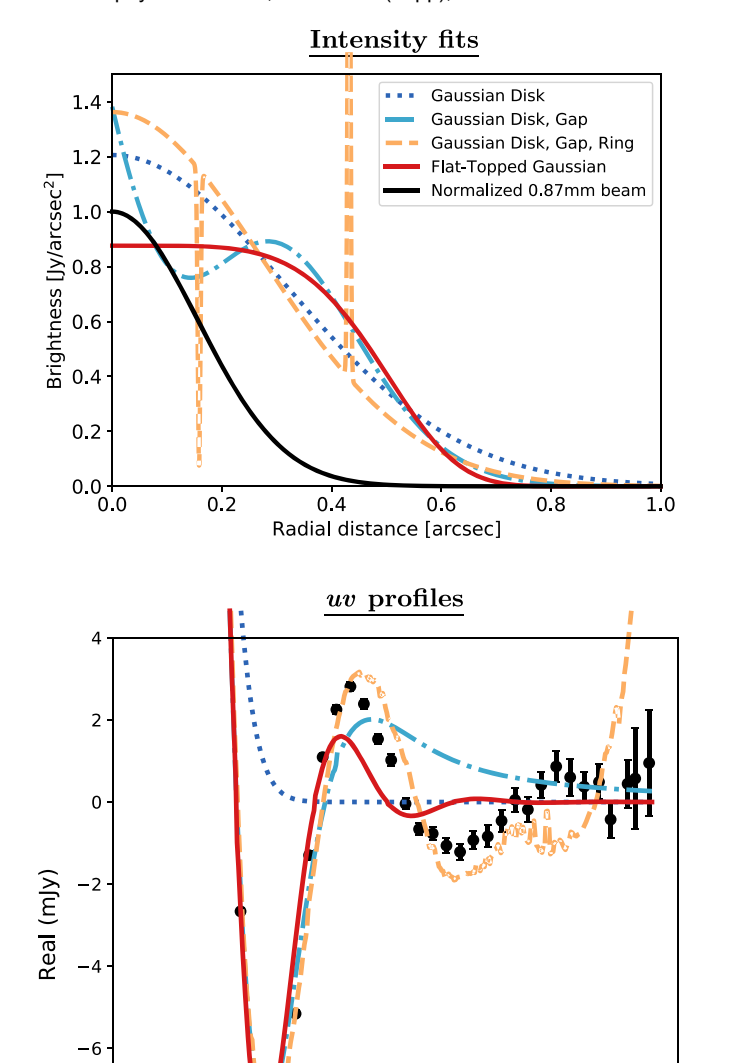


Figure 4. The variety of morphologies from the best-fit geometric models for the 0.87 mm data are shown hereop: the intensities as a function of radial distance are shown. The solid black curve represents the normalized 0.87 mm circularized Gaussian beam, thus illustrating the approximate image resolution. Bottom: the corresponding uv profiles of the best-fit geometric models at 0.87 mm with the observations plotted in blackThese are the same profiles shown as red lines in the right-most panels of Figure 2.

uv-distance (kλ)

600

-8

-10

200

400

0.87 mm data Gaussian disk

Gaussian disk, gap Gaussian disk, gap, ring Flat-Topped Gaussian

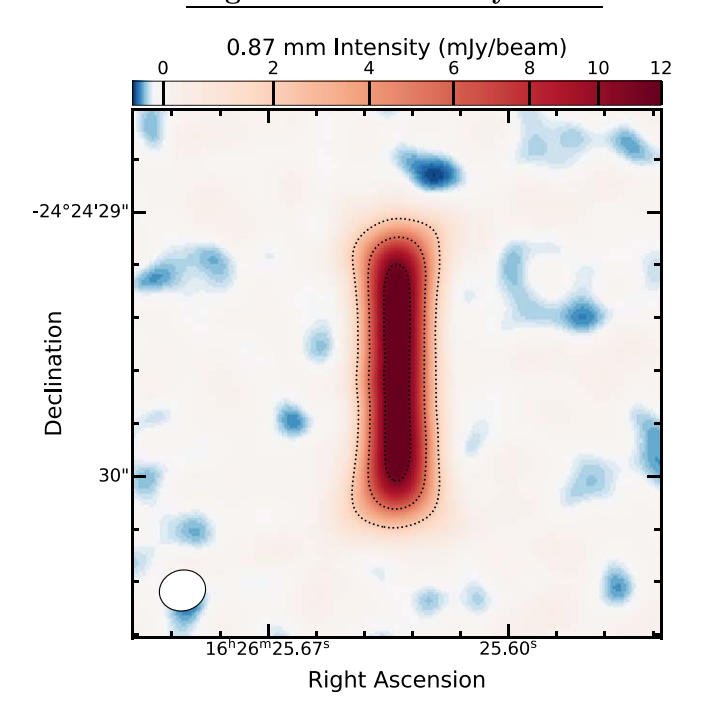
1000

800

1200

observations rather we are making a qualitative comparison. While the residuals show qualitatively similar positive and negative residuals along the north and south, we subtract slightly too much emission along the major axis and not enough emission along the minoaxis. Since the toy model assumes a perfectly edge-on FTG disk input/whereas VLA 1623W's disk inclination is ~80°, some of these differences could be the effect of inclination. In addition, the toy model is a The black contours represent ±3, 10, and 20 of residuals. simple approximation of the dust emission, whereasa full description would require radiative transfer modeling and directly fitting for the disk structure simultaneously, especially as we would anticipate a change in optical depth and

## Edge-on flared disk toy model



#### Residuals

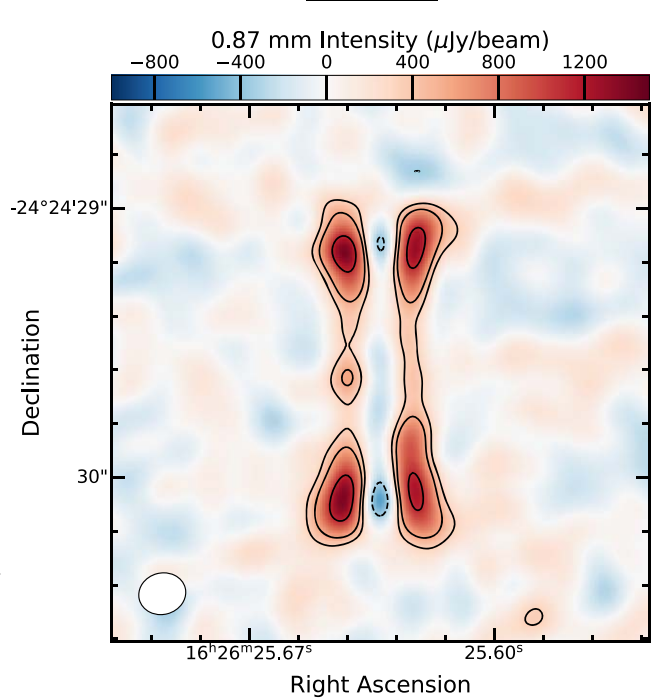


Figure 5. Top: simulated observations at 0.87 mm of the flaredge-on disk toy model image using the same observational conditions as VLA 1623W. The parameters used are n = 4 au,  $n_0 = 0.1$ ,  $\beta = 5$ , and  $n_0 = 30$  au. The black dotted lines represent the contours of the 0.87 mm model disk emission at 20, 50, and 100 g. Bottom: imaged residuals after the subtraction of the Fourier transform of the best-fit FTG model from the simulated observations of the toy model (top panel). These imaged residuals correspond to the centramelin Figure 10 as it is the qualitatively most similar to the observation's residuals.

temperature from the midplane to the flared edges and there may be non-negligible contributions to the intensity from scattered emission. Such 3D radiative transfer models are

beyond the scope of this work but will be necessary to evaluate bservations, implying that large dust grains are elevated above the features seen in VLA 1623W fully.

#### 4. Discussion

From our modelfits and toy model, we propose that VLA 1623W is indeed a protostellar disk and thathe disk is both optically thick and flared. The lack of a large envelope feature (Murillo & Lai 2013; Kirk et al. 2017), suggeststhat the millimeter emission purely traces the disk. Within the VLA 1623 protostellar system, both the VLA 1623Aa & Ab canonical protobinary and VLA 1623B are considered Class 0 sources. VLA 1623W, however, has been labeled as a Classscattering and optical depth (Tazzari et aD18). In Figure 3, source based on its spectral energy distribution and its envelope-to-stamass ratio (Murillo & Lai 2013; Murillo et al. 2018). Harris et al. (2018) find that West could have beerconsistently brighter by a factor of ~2 compared to the ejected from the triple system VLA 1623Aa, Ab, & B based on equivalent locations on the western side. a proper motion analysis, thus possibly implying a common age. In an ejection scenario, the envelope could be stripped such that only the disk survives (Reipurth 2000). The failure of the eastern side is the far side of the disk, we may be observing the models that include an envelope component (e.g., the PLCTassively heated dust in the flared disk whereas for the western model; see Section 2.2) suggeststhere is no significant envelope in these deep mm observations eith@e acknowledge that the envelope component could be encapsulated at u2022b). Alternatively, VLA 1623W has detected polarized distances <50 kλ.To investigate this furtherwe fit the PLCT model to data sets where VLA 1623Aa,Ab, & B have been subtracted but still contain the full uv range. The same result isbe a flux enhancementn the direction of forward scattering found as with the 50 kλ cut data where the PLCT model turns over backward scattering (e.g.errin etal. 2015; Yang et al. to a Gaussian disk model with no envelope being found at both2017). In this scenario the brighter eastern side would be the 1.3 and 0.87 mm. Thus, VLA 1623W could be as young as the nearside of the disk. Thus, temperature and scattered light VLA 1623Aa, Ab, & B sources but simply lacks an envelope due to it having been dynamically ejectedUltimately, VLA 1623W's exact classification is not clear, but it is likely of similar age to the VLA 1623AaAb, & B system.

#### 4.1. Vertical Settling

The disk flaring observed in millimeter dust for VLA 1623W implies that the disk's outer edges are still significantly puffed up with vertically distributed mm-dust above the cold disk midplane. This dust has not yet completely settled onto a thin disk. In general, vertical settling is observed in the difference in Further work, constraining the rate at which the millimeterscale heights between the infrared and millimeter-sized dust insized dust concentrates in the midplane is important to the protoplanetary disk observations (e.gV,illenave et al. 2020; Miotello et al. 2022). The small micron-sized dust follows the higher gas scale height whereasthe millimeter-sized dust appears to be well settled in the midplane (Barrière-Fouchet et al. 2005).

for some Class II protoplanetary disks (e. bl. Tau, 2MASS J16083070-3828268, Tau 042021, SSTC2DJ163131.2-242627constrained. and Oph 163131; Pinte et al. 2016; Villenave et al. 2019, 2020; Wolff et al. 2021; Villenave et al. 2022). By contrast, some disks and/or parts of disk substructures have been found to show elevated millimeter dust vertical scale heights. For example, HD 163296, a Class II disk where Doi & Kataoka (2021) find both settled and puffy dustings, IRAS 04302, a Class I protostellar disk where Villenave at. (2020) suggest that it may be flared and less settled, and the Class 0 protostellaruum observations at different wavelengthsprovides an source HH 212, which exhibits hamburger-shapemission indicative of unsettled millimeter-sized dustee et al. 2017). Both Ohashi et al. (2022b) and Sheehan et al. (2022) report flaring for the edge-on Class 0 disk L1527 IRS in millimeter

the disk midplane. These observations seem to indicate that some protostellardisks may be puffed up with longer dustsettling timescales. For example, significant turbulence may stir up large dust (Sheehan et al. 2022).

The current methodology used provides a good firstook into VLA 1623W's morphology and its features. We highlight the uniqueness of finding possible flaring in a Class 0/I disk, adding to the small sample of protostellar disks known to exhibit similar behavior (HH 212 and IRAS 04302; Lee et al. 2017; Villenave et al. 2020). Furthermore, the high inclination challengesthe analytic profiles which do not account for we may be seeing some of these effects as the residuals in the north and south corners of the eastern side of the disk are

This difference in brightness could imply that the eastern side is slightly warmer than the western side or example if side (nearside) the disk may be shadowed by the cooler outer edge of the flare (e.g., similar to L1527 IRS; Ohashi et al. light of order 1%-1.5% (Harris et al. 2018; Sadavoy et al. 2019). If the polarization is from dust self-scattering, there will present competing effects that may both be present. 3D radiative transfer calculations with a flared disk model will be necessary to discern the reason for the east-westresidual asymmetry.

The toy model is not designed to reproduce the observations. We emphasize that we are notaining to quantitatively fitthe toy model to the data butrather we qualitatively compare the residuals using an identicabrocedure. From the results (see Figures 3 and 5), the residuals' morphological imilarities are striking and thus appear as a possible solution to VLA 1623W disk's features.

description of the initial conditions for planet formation given that dust densities are a crucial component to trigger this process (Drazkowska et al. 2022; Miotello et al. 2022). Observing a larger sample of edge-on protostellardisks to connect with Villenave et al. (2020)'s protoplanetary disks Vertical settling into a very thin dust disk has been observed would allow for a more accurate evolutionary picture if the disk kinematics and envelope components can be properly

### 4.2. Spectral Index Map

From the polarization results we worked with the assumption that VLA 1623W is optically thick for the disk modeling. Now, with the two wavelengths available, we can test this assumption independently The ratio of the millimeter conestimation of the spectral index  $\alpha_{mm}$  as  $S_n \mu n^{a_{mm}}$ . Across disks,  $\alpha_{mm}$  has been used to constrain the dusptical depth and consequently describe the dust grain sizes; however, these are degenerate (Williams & Cieza 2011; Miotello et al. 2022).

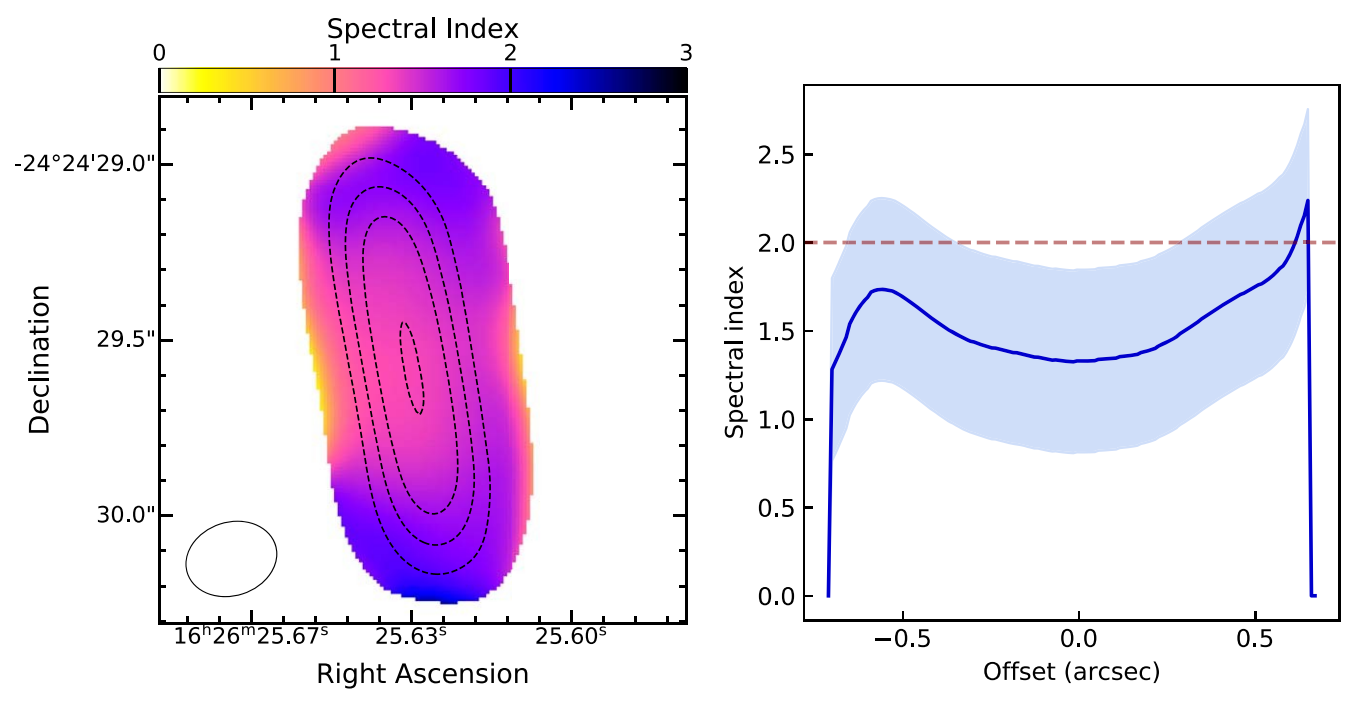


Figure 6. Left: map of spectral index for the region where the intensity is greater than 10 σ both in Bands 6 and 7. The dotted lines represent the contours of 0.87 n disk emission of VLA 1623W at 20, 50, 100, and 290smoothed to the same resolution as the spectral index map. Right: spectral index along the disk's major axis. The x-axis is the offset from the disk center, and from the FTG fits, we find \( \partial \text{0}'\)45-0 \( \frac{4}{6}\). The shaded light blue is the spectral index evaluated assuming a 10% flux uncertainty from the calibration for both 1.3 and 0.87 mm data.

The dust opacity is expected to have a power-law dependencytracing the outermostlust surface layer of an optically thick Jeans regime such that  $\kappa v^{\beta}$ , where  $\kappa$  is the dust absorption coefficient and  $g_m = \beta + 2$  at the Rayleigh–Jeans limit (where  $h_v/kT \ll 1$ ) such that optically thick dust has  $g \rightarrow 2$  or large grains that have  $\beta = 0$ .

We measured the q<sub>m</sub> map using the Stokes Icontinuum to the best-fit FTG model offsets obtained at each wavelength by Miotello et al. 2022), which given the high inclination of We clean the observations with uniform weighting across the same uv range (17–1700 kλ) and smoothed each map by the beam of the other so that the two images have a common resolution of 026 × 0.121. To focus on the main disk emission, we mask outemission <10 σ atboth wavelengthsUsing the immath task in CASA, we evaluate the spectraindex map pixel-by-pixel from the two wavelength observations.

Figure 6 (left) shows the Am map with dashed contours of the VLA 1623W disk emission at 0.87 mm and (right) the radial profile of the q<sub>m</sub> along the disk's major axis. We find a global spectralindex of 1.5 ± 0.2 consistent with a high dust optical depth across the disk and possibly lower than edge-on protoplanetary diskse.g., the median  $q_{nm}$  of 2.5 ± 0.3 from Villenave et al. (2020). The value of  $\alpha_{mm}$  increases radially along the disk's major axis, similar to that found by Villenave et al. (2020). Generally, we find that VLA 1623W is consistent ringing into the uv visibilities that can mostly fit the with being optically thick throughout most of the disk.

The optically thick dust result from the polarization and α data are consistenwith the FTG description, which implies a center. We are observing the outerregion of the disk more uniformly. This is particularly visible along the disk's major due to the high inclination along the line of sight. Modeling the 2018; van der Marel et al2021), there is the need to identify

at millimeter frequencies which corresponds to the Rayleigh- source. Note that for some protoplanetary disks, Villenave et al. (2020) report similar sharp edgesin the brightness profiles along the disk's major axis.

It must be noted that a further nuance exists with such inclined protostellardisks, which is the effect of scatteringinduced intensity reduction along the disk midplane and observations at 1.3 and 0.87 mm. We center the disks accordingssible enhancements in the puffy outer edges (see the review VLA 1623W, can impact the derived millimeter spectral index by decreasing the intensity in the optically thick region further (Zhu et al. 2019; Sierra & Lizano 2020). Furthermore low protostellar disk temperatures in the outer layers due to selfobscuration will also contribute to decreasing the spectral index (Zamponi et al.2021).

#### 4.3. No Disk Substructure

We favor the FTG modebver the more complex Gaussian disk, gap, ring model even though the latter produced a statistically superiorfit to the observations at 0.87 mm. As discussed in Section 3.3, the best-fit parameters for the Gaussian disk, gap, ring profile required a sharp gap and sharp ring that are well below the current observation's resolution (see Figure 4). These sharp features artificially introduce observations butnay instead be artifacts rather than redisk substructures.

These results indicate the dangers of overinterpreting constant surface brightness across the disk, rather than a peakeducture in young and inclined protostellar disks. As structured disks have been readily observed athe Class II stage (e.g., ALMA Partnership et al. 2015; Andrews et al. 2016; Isella axis, which we are probing in better detail than the minor axis, et al. 2016; Andrews et al. 2018; Huang et al. 2018; Long et al. disk according to this prescription implies that we are primarily the precursors to such features in younger disks, namely in the protostellar Class 0/I stages. Some young, large, massive protostellar disks have indeed been observed to have substructure,including IRS 63 in Ophiuchus (Segura-Cox et al. 2020). L1489 IRS (Ohashi et al2022a), and a series of Class 0/I disks in Orion (Sheehan et al. 2020). As the community searches for the precursors of the highly structured We thank the anonymous referee for their constructive and disks found in the DSHARP sample, for example (Andrews et al. 2018; Huang et al. 2018), we must be wary of the evidence and models presented The models presented here represent simple 1D geometric profiles that cannot fit complex and Engineering ResearchCouncil of Canada (NSERC). disks with flared structures wellAs a further testof the disk models, we also use a nonparametric approach by fitting the data sets with frank (Jennings et al.2020). The results from frank suggest a highly structured protostellar disk, see Figure 13 in Appendix A3, that is most similar to the Gaussian NSC and ASIAA (Taiwan) and KASI (Republic of Korea), in disk, gap, ring model in Section 3.1. However, it is difficult to compare the modelfits quantitatively and statistically across both codes. Given that we reject GALARIO's complex Gaussian, disk, gap, ring model, we are also inclined to disfavor frank's highly structured disk. Both codes are limited to geometrically thin disks, whereas VLA 1623W appears more complex. Ultimately, 3D radiative transfer modeling will be necessary to capture the structurertical extent, and optical properties of this source.

#### 5. Conclusions

We fit VLA 1623W 1.3 and 0.87 millimeter observations using simple geometric models to determine if this source is consistentwith standard disk models. Our main results and interpretations are as follows:

- 1. VLA 1623W is consistent with being a young protostellar disk. It is highly inclined, optically thick, and wellcharacterized by a modified FTG, indicating that the emission is relatively constantlong the major axis and not peaked.
- 2. We find similar positive residuals athe four corners of morphology is well matched by a toy model of an edgemay not have had time to settle onto a thin midplane.
- 3. For protostellar sourcestructured real uv visibilities do not necessarily imply substructure.

This study takes advantage of the high-sensitivity Stokes I continuum data from polarization observations of disks (Harris et al. 2018; Sadavoy et al. 2019). The ability to discern subtle and provide further details as to its designection 3.3 briefly hints in the disk morphology such as flaring and rule outle presence of substructure is instrumeritabur descriptions of protostellardisks. Protostellardisk polarization observations thus support this goal in addition to constraining the dust grain produced residualsWe also note that the parameters being sizes (Kataoka et a2015).

If VLA 1623W is confirmed to be flared from future millimeter wavelengths at high resolution and sensitivityen it will provide an interesting laboratory to study dust settling as well as dust grain properties across the vertical disk scale height in protostellar source and could add to the sample of known young puffed-up disks at millimeter wavelengths (e.g., profile according to the 0.87 mm FTGt,fi HH 212 and I1527; Lee et al. 2017; Ohashi et al. 2022b; Sheehan et al. 2022). In turn, this would provide constraints on the dust-settling rates from protostellar to protoplanetary disks, setting the stage for comparisons with highly settled Class II disks (Villenave et al. 2022). As we continue to search for the

initial precursorsto disk substructure and aim to constrain planet formation's initial conditions, we must further enlarge our sample of protostellar disks at high resolution and sensitivity.

useful suggestions. The authors are grateful to Luca Matrà and Marco Tazzari for helpful discussions in running GALARIO. A. M. and S.I.S.acknowledge supporfrom the Natural Science RGPIN-2020-03981. L.W.L. acknowledges support from NSF AST-1910364 and NSF AST-2108794. ALMA is a partnership of ESO (representing its member states), NSF (USA) and NINS (Japan),togetherwith NRC (Canada) and cooperation with the Republic of Chile. The Joint ALMA Observatory is operated by ESOAUI/ NRAO and NAOJ. This paper makes use of the following ALMA data: 2015.1.01112.S and 2015.1.00084.S.

Software: CASA (McMullin et al. 200,7GALARIO (Tazzari et al. 2018), emcee (Foreman-Mackey et al. 2013), matcorner (Foreman-Mackey 2016), plotlib (Hunter 2007), APLpy (Robitaille & Bressert 2012).

#### **Appendix**

#### A1. Best-fit Geometric Disk Model Beam-convolved Images

In this section, we present images of the best-fit disk models from Table 1. Figure 7 shows images of the disk models convolved with the beam at 1.3 mm and 0.87 mm. The Gaussian disk model is the only one from the selection which differs slightly qualitatively from both the observations and the other disk models. The other three models are virtually indistinguishable from each other and the observations when convolved with the beam at both wavelengths. Figure 8 shows the radial profiles of the imaged models and demonstrates the similarity between the modeled data when convolved with the the disk for various models and at both wavelengths. Thisbeam compared to the original unconvolved models in Figure 4. We note that the observed image at 0.87 mm does on flared disk. Thus, the large dust grains in VLA 1623W appear a bit boxier than the modeled data, however. This shape may reflect the flared nature of the disk, which is not captured in the geometrically thin modeled data.

#### A2. Edge-on Flared Disk Toy Model

In this section, we test the parameter space for the toy model describes the toy modeland shows the resultof one of the better models matching the observations. We do not fit the observations, but we show representative images of the tested are not motivated by radiative transfer; this is a qualitative resultused to provide a suggested explanation for the systematic residuals observed in Figure 3.

We base the toy model disk on the FTG model and supplement this with a flaring shape. For simplicity, we model the disk with  $i = 90^{\circ}$  and PA =  $0^{\circ}$  and generate the intensity

$$I_1(R) = I_0 \exp\left(-0.5\left(\frac{R}{s_0}\right)^r\right),$$
 (A1)

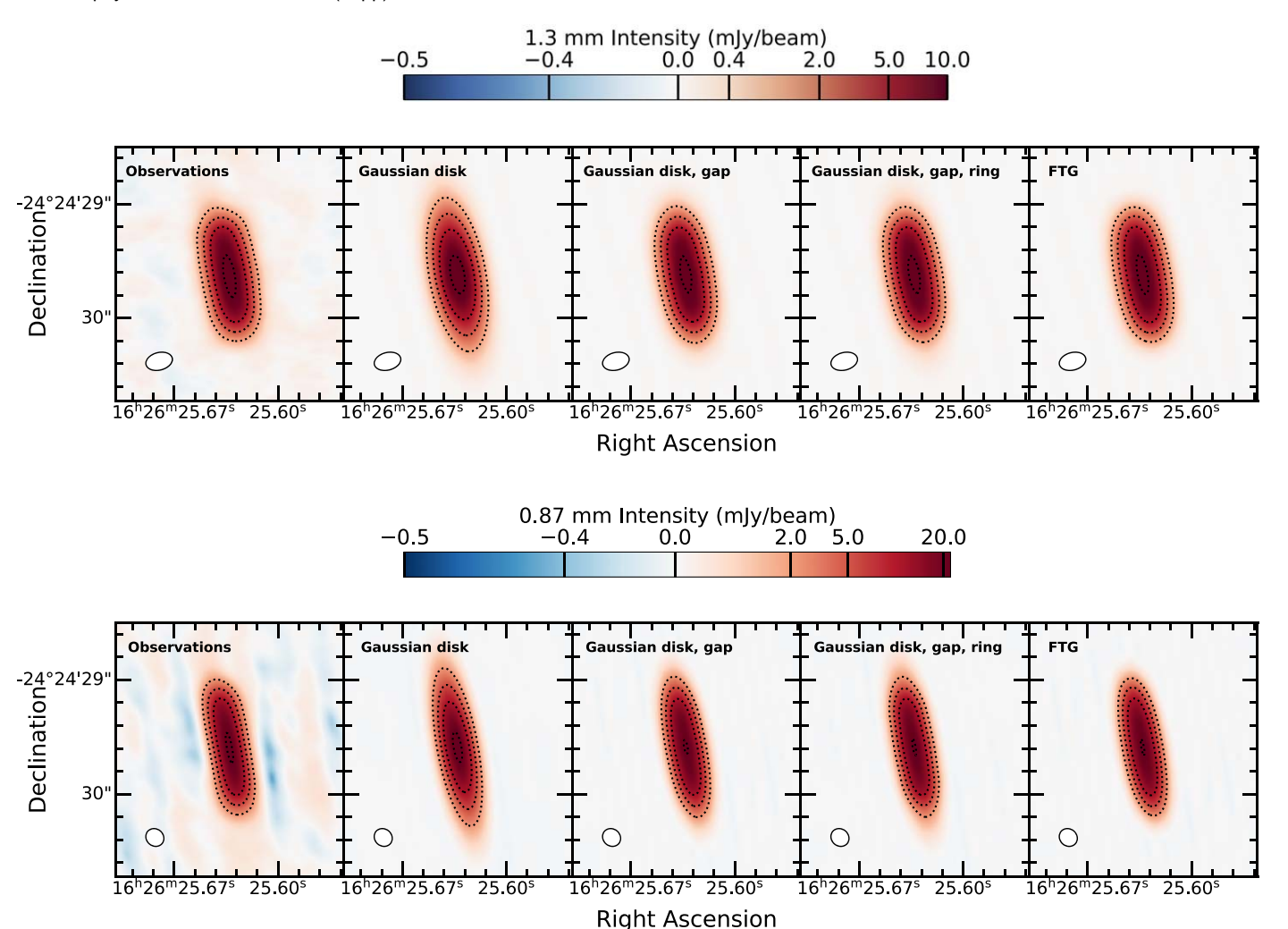


Figure 7. Images of the best-fit disk models compared to the observations (leftmost panel). The model images were obtained by taking the Fourier transform of the best-fit disk model image and sampling the uv plane of the observations using GALARIQ.at 1.3 mm and Bottom: at 0.87 mm.

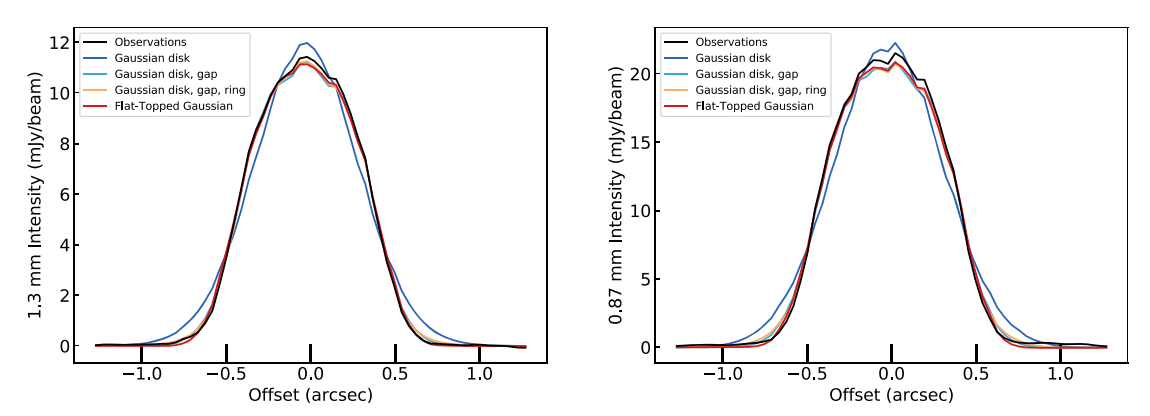


Figure 8. Intensity profiles along the disk major axis of the best-fit disk model images presented in Figure 7. The best-fit disk profiles prior to the uv plane sampling Fourier transformation and beam convolution are shown in Figure 4eft: at 1.3 mm and Right: at 0.87 mm.

where  $I_0 = 18.4$  mJy beam<sup>-1</sup>,  $\sigma_0 = 0.40$ , and f = 5.0. To The value of  $\sigma_h(R)$  is modeled according to a verticalisk model the flaring, we use a Gaussian function whose width,  $\sigma$  extent function described in Equation (2). We provide the will change as R increases away from the disk center such that equation for  $\sigma_h(R)$  again below for the reader,

$$I_2(R) = I_1(R) \exp\left(-0.5\left(\frac{R}{s_1(R)}\right)^2\right).$$
 (A2)  $s_1(R) = h_0\left(\frac{R}{R_0}\right)^6 + h_{\text{off}}.$ 

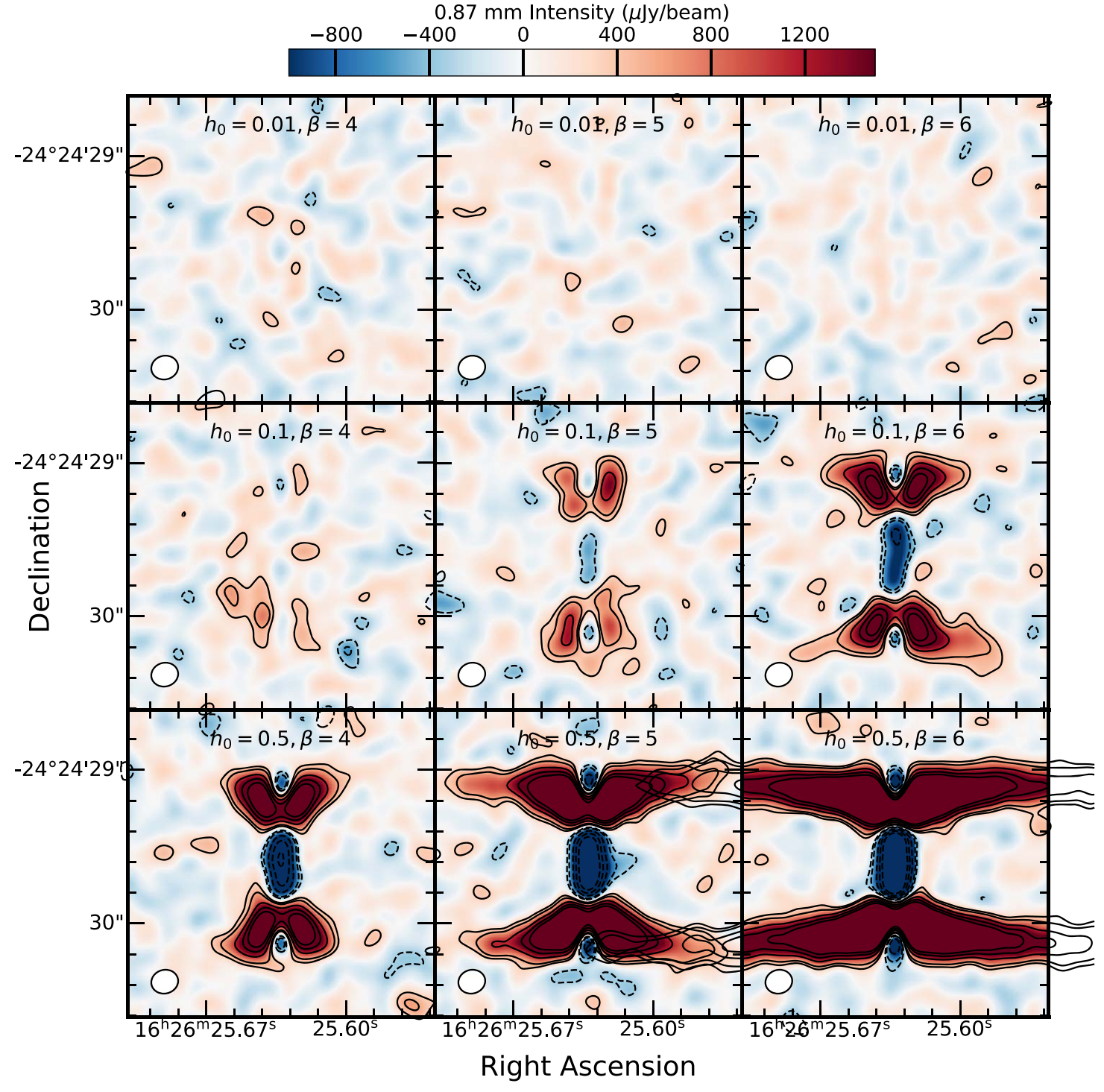


Figure 9. The parameters used to generate the flared disk models for this gright ar θ bu and R = 30 au, where we explore the effect of changing and β. The black contours represent ±35, 10, 15, and 20  $\sigma_r$  residuals.

With the generated disk intensity image, we simulate ALMA 0.87 mm observations using simalma with an identical setup as the 0.87 mm observations (Harris et 2018), then we use GALARIO to recover the best-fit FTG model, and we evaluate  $h_0 = [0.1, 0.5]$ , and  $h_{off} = 4$  au. The bottom grid in Figure 12 the residuals.

We manually conduct a small parametersearch to find reasonable fits that yield similar residuals to those obtained from the observations. We examine the effects of varying h h<sub>off</sub>, and R₀ on the resulting residuals.

Figures 9–11 show the residuals for fixed R= 30 au with  $\beta = [4, 5, 6], h_0 = [0.01, 0.1, 0.5], and h_{ff} = [3, 4, 5] au$ . The top grid in Figure 12 shows  $R_0 = 10$  au with  $\beta = [0.5, 1]$ , shows  $\Re$ = 50 au with  $\beta$  = [5, 7],  $\theta$ = [0.5, 1], and  $\theta_{ff}$  = 4 au. For the smaller grids, of is fixed at 4 au, motivated by the best residual from the R= 30 au grid. The two grids at R= 10 au and  $R_0 = 50$  au are smaller to illustrate the effects of changing  $R_0$ , although we note that  $h_0$  and  $\beta$  required different ranges

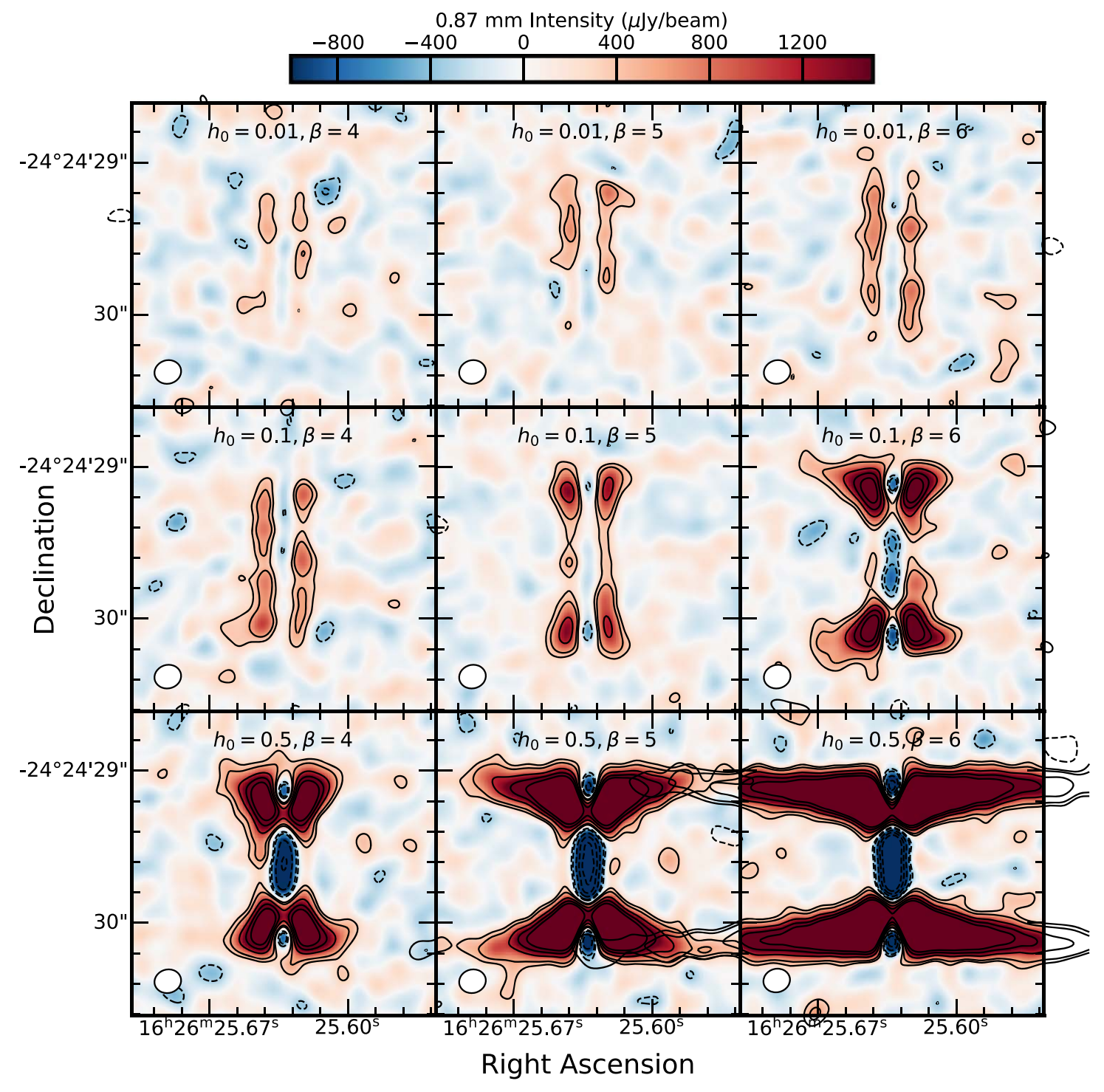


Figure 10. Same as Figure 9 but for this grid we use #= 4 au.

from the  $R_0$  = 30 au case to keep the toy model generally consistent with the observations.

In general, for the  $R_0$  = 30 au cases,the smallestvalue of  $h_0$  = 0.01 produces disks with insufficienflaring resulting in residuals (<3  $\sigma_7$  in most cases) that do not match the observations residuals. The highest value of  $h_0$  = 0.5 tested produces too much flaring for all cases examined Similarly, most of the models with low  $\beta$  = 4 or high  $\beta$  = 6 produce too little or too much flaring, respectively. Thus, the best-fit cases are with  $h_0$  = 0.1 and  $\beta$  = 5 for the grids examined in

Figures 9, 10, and 11. We note that there are slight differences with  $h_{off}$ , where there is too much angled flaring fq<sub>ff</sub>  $\not\models$  3 au and a stronger centrabridge and more box-like residuals for  $h_{off} = 5$  au. Thus, we identify the best match to the observations based on visual inspection to be the  $h_0 = 0.1$ ,  $\beta = 5$ , and  $h_{off} = 4$  au model for  $P_0 = 30$  au (see also Figure 5).

In Figure 12, we show the results of adjusting the scaling radius  $R_0$ . For  $R_0$  = 10 au (see the top grid of Figure 12)the residual flaring starts too close to the inner disk region compared to the observation of  $R_0$  = 50 au (bottom grid of

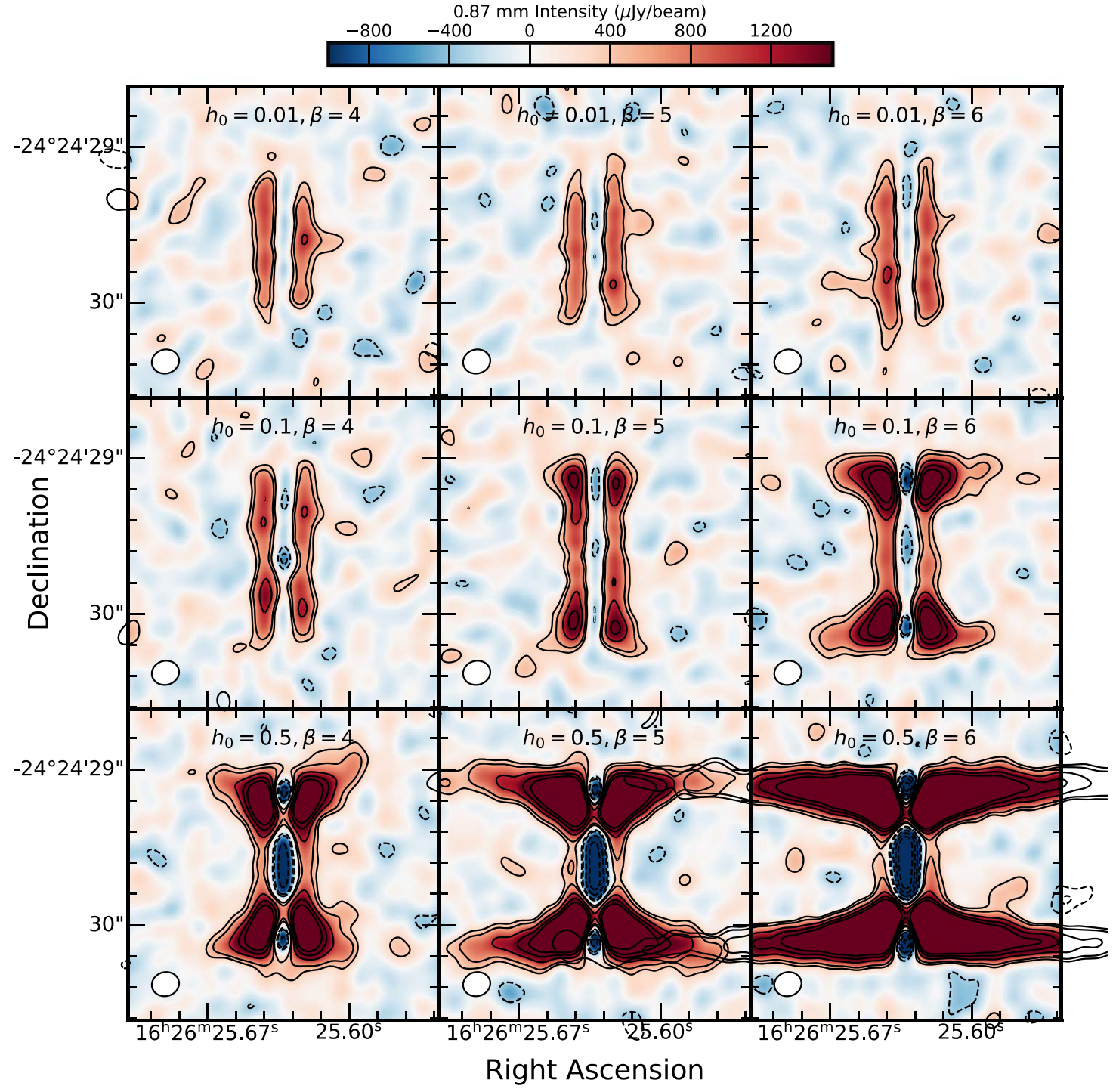


Figure 11. Same as Figure 9 but for this grid we use fig = 5 au.

Figure 12), the flaring is restricted to the outer disk as seen in the observations, and these toy models are comparable to those We run frank from Jennings et al. (2020) for both 50 kλ from the R<sub>0</sub> = 30 au grid. Further parameter fine tuning will be necessary to constrain the actualisk and flaring properties. The ideal radial scaling could be between  $30_0 \square 100$  au with  $h_0$  and  $\beta$  being adjusted accordingly. There is an upper limit of and a ring feature over the underlying disk at 1.3 mm and R = 100 au given that the disk radius is smaller than that this paper, we select  $R_0 = 30$  au as a good approximation for the radial scaling factor.

#### A3. Testing frank

cut data sets providing the source coordinates, inclination, and PAs from the GALARIO-inferred FTG fits In both cases the resulting inferred disk is highly structured and includes a gap possibly two rings and a gap in the 0.87 mm data, see Figure 13. This highlights the dangers of overinterpreting features found in the uv visibilities for highly inclined sources.

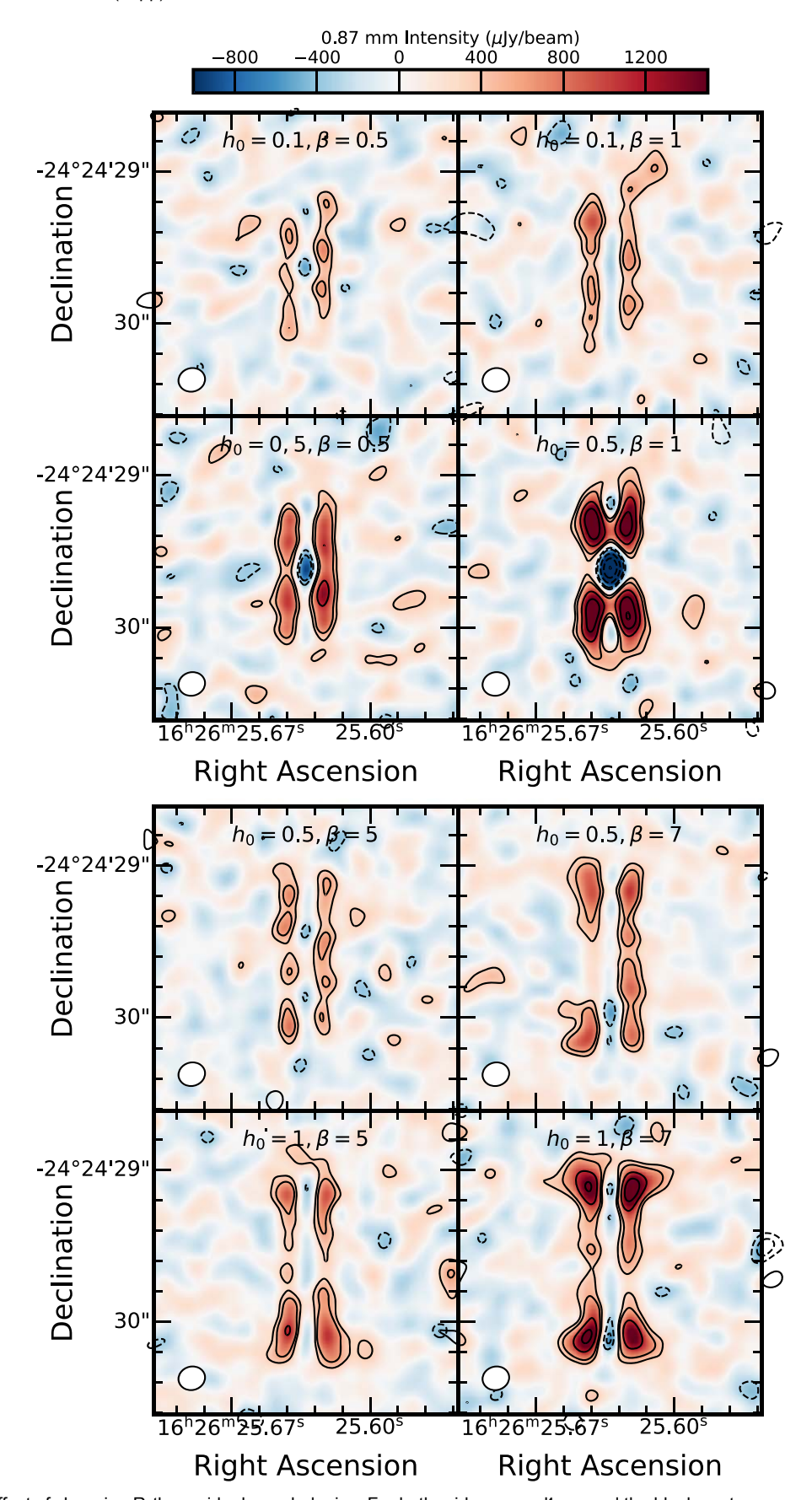


Figure 12. Testing the effect of changing  $\sigma$  the residual morphologies. For both grids we use  $rac{1}{2}$  au, and the black contours represent  $\pm 3$ , 5, 10, 15, and 20  $\sigma$  residuals. Top grid: we use  $rac{1}{2}$  10 au with varying  $rac{1}{2}$  and  $rac{1}{2}$  10 au with varying  $rac{1}{2}$  and 30 au.

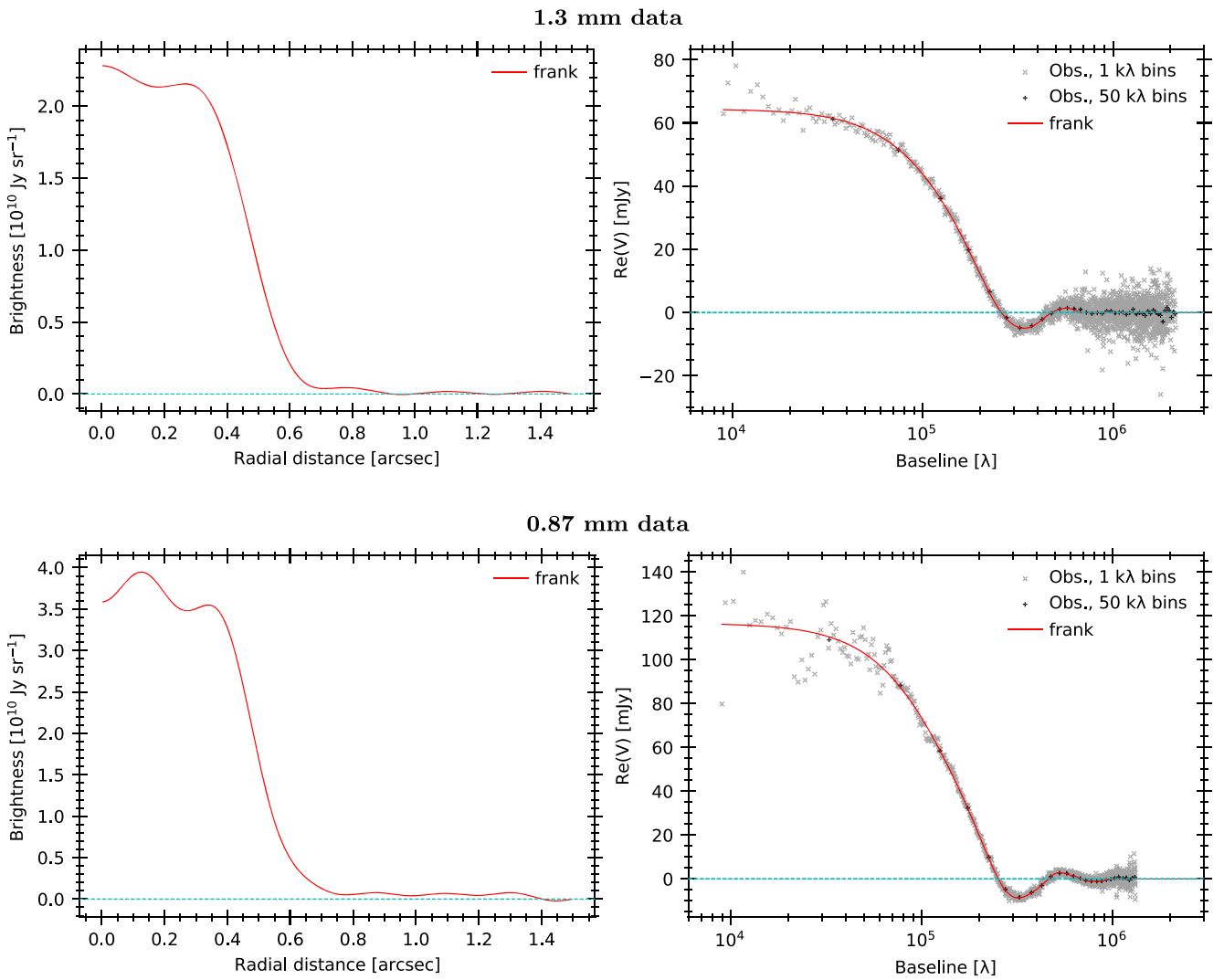


Figure 13. Brightness and real uv profiles for the frank fits to both data sets. In the top row the 1.3 mm data are fit and in the bottom row the 0.87 mm data are fit.

It is qualitatively similar to whatwe found from the complex Gaussian disk,gap, ring model with GALARIO, which we disfavor compared to the FTG modelJennings etal. (2020) does highlight frank's limitations including the challenges of modeling disks with high inclination, optical depth, or vertical structure. VLA 1623W has all of these features, so an overinterpretation of structure is not unexpected.

## ORCID iDs

Arnaud Michel® https://orcid.org/0000-0003-4099-9026
Sarah I.Sadavoy® https://orcid.org/0000-0001-7474-6874
Patrick D.Sheehar® https://orcid.org/0000-0002-9209-8708
Leslie W. Looney® https://orcid.org/0000-0002-4540-6587
Erin G. Cox ® https://orcid.org/0000-0002-5216-8062

#### References

Akaike, H. 1974, ITAC, 19, 716
ALMA Partnership, Brogan, C. L., Pérez, C. L., et al. 2015, ApJL, 808, L3
Andre, P., Martin-Pintado, J., Despois, D., & Montmerle, T. 1990, A&A, 236, 180
Andre, P., Ward-Thompson, D., & Barsony, M. 1993, ApJ, 406, 122
Andrews, S. M., Wilner, D. J., Zhu, Z., et al. 2016, ApJL, 820, L40
Andrews, S. M., Elder, W., Zhang, S., et al. 2021, ApJ, 916, 51

Andrews, S. M., Huang, J., Pérez, L. M., et al. 2018, ApJL, 869, L41 Andrews, S. M., Wilner, D. J., Hughes, A. M., Qi, C., & Dullemond, C. P. 2009, ApJ, 700, 1502 Barrière-Fouchet,L., Gonzalez, J. F., Murray, J. R., Humble, R. J., & Maddison, S. T. 2005, A&A, 443, 185 Bontemps, S., & Andre, P. 1997, Poster ProcIAU Symp. 182, Herbig-Haro Flows and the Birth of Low Mass Stars, Vol. 182 ed. F. Malbet & A. Castets (Berlin: Springer), 63 Boyden, R. D., & Eisner, J. A. 2020, ApJ, 894, 74 Caratti o Garatti, A., Giannini, T., Nisini, B., & Lorenzetti, D. 2006, A&A, 449, 1077 Cridland, A. J., Rosotti, G. P., Tabone, B., et al. 2022, A&A, 662, A90 Dent, W. R. F., Matthews, H. E., & Walther, D. M. 1995, MNRAS, 277, 193 Doi, K., & Kataoka, A. 2021, ApJ, 912, 164 Drazkowska J., Bitsch, B., Lambrechts M., et al. 2022, arXiv:2203.09759 Eisner, J. A., Arce, H. G., Ballering, N. P., et al. 2018, ApJ, 860, 77 Esplin, T. L., & Luhman, K. L. 2020, AJ, 159, 282 Evans, N. J. I., Dunham, M. M., Jørgensen, J. K., et al. 2009, ApJS, 181, 321 Foreman-MackeyD. 2016, JOSS, 1, 24 Foreman-MackeyD., Hogg, D. W., Lang, D., & Goodman, J. 2013, PASP, 125,306 Greene, T. P., Wilking, B. A., Andre, P., Young, E. T., & Lada, C. J. 1994, ApJ, 434, 614 Gulick, H. C., Sadavoy, S., Matrà, L., Sheehan, P., & van der Marel, N. 2021, ApJ, 922, 150 Hara, C., Kawabe, R., Nakamura, F., et al. 2021, ApJ, 912, 34 Harris, R. J., Cox, E. G., Looney, L. W., et al. 2018, ApJ, 861, 91

Huang, J., Andrews, S. M., Dullemond, C. P., et al. 2018, ApJL, 869, L42

```
Hunter, J. D. 2007, CSE, 9, 90
Isella, A., Guidi, G., Testi, L., et al. 2016, PhRvL, 117, 251101
Jennings, J., Booth, R. A., Tazzari, M., Rosotti, G. P., & Clarke, C. J. 2020,
            , 495, 3209
Kass, R. E., & Raftery, A. E. 1995, J. Am. Stat. Assoc., 90, 773
Kataoka, A., Muto, T., Momose, M., et al. 2015, ApJ, 809, 78
Kawabe, R., Hara, C., Nakamura F., et al. 2018, ApJ, 866, 141
Kirk, H., Dunham, M. M., Di Francesco, J., et al. 2017, ApJ, 838, 114
Lee, C.-F., Li, Z.-Y., Ho, P. T. P., et al. 2017, SciA, 3, e1602935
Long, F., Pinilla, P., Herczeg, G. J., et al. 2018, ApJ, 869, 17
Looney, L. W., Mundy, L. G., & Welch, W. J. 2000, ApJ, 529, 477
Lynden-Bell, D., & Pringle, J. E. 1974, MNRAS, 168, 603
Maury, A., Ohashi, N., & André, P. 2012, A&A, 539, A130
McMullin, J. P., Waters, B., Schiebel, D., Young, W., & Golap, K. 2007, in
   ASP Conf. Ser. 376, Astronomical Data Analysis Software and Systems
   XVI, ed. R. A. Shaw, F. Hill, & D. J. Bell (San Francisco, CA: ASP), 127
Miotello, A., Kamp, I., Birnstiel, T., Cleeves, L. I., & Kataoka, A. 2022,
  arXiv:2203.09818
Murillo, N. M., Harsono, D., McClure, M., Lai, S. P., & Hogerheijde, M. R.
   2018, A&A, 615, L14
Murillo, N. M., & Lai, S.-P.2013, ApJL, 764, L15
Murillo, N. M., Lai, S.-P., Bruderer, S., Harsono, D., & van Dishoeck, E. F.
   2013, A&A, 560, A103
Nakamura, F., Kamada, Y., Kamazaki, T., et al. 2011, ApJ, 726, 46
Nisini, B., SantangeloG., Giannini, T., et al. 2015, ApJ, 801, 121
Ohashi,S., Codella,C., Sakai,N., et al. 2022c,ApJ, 927,54
Ohashi,S., Kobayashi,H., Sai,J., & Sakai, N. 2022a,ApJ, 933, 23
Ohashi, S., Nakatani, R., Liu, H. B., et al. 2022b, ApJ, 934, 163
```

Ortiz-León, G. N., Loinard, L., Dzib, S. A., et al. 2018, ApJL, 869, L33
Pattle, K., Ward-Thompson, Kirk, J. M., et al. 2015, MNRAS, 450, 1094

```
Perrin, M. D., Duchene, G., Millar-Blanchaer, M., et al. 2015, ApJ, 799, 182
Pinte, C., Dent, W. R. F., Ménard, F., et al. 2016, ApJ, 816, 25
Reipurth, B. 2000, AJ, 120, 3177
Robitaille, T., & Bressert, E. 2012, APLpy: Astronomical Plotting Library in
   Python, Astrophysics Source Code Librargscl: 1208.017
Sadavoy,S. I., Myers, P. C., Stephensl. W., et al. 2018, ApJ, 859, 165
Sadavoy,S. I., Stephensl. W., Myers, P. C., et al. 2019, ApJS, 245, 2
SantangeloG., Murillo, N. M., Nisini, B., et al. 2015, A&A, 581, A91
Schwarz, G. 1978, AnSta, 6, 461
Segura-Cox, D. M., Schmiedeke, A., Pineda, J. E., et al. 2020, Natur, 586, 228
Sheehan P. D., Tobin, J. J., Federman S., Megeath, S. T., & Looney, L. W.
   2020, ApJ, 902, 141
SheehanP. D., Tobin, J. J., Li, Z.-Y., et al. 2022, ApJ, 934, 95
Sierra, A., & Lizano, S. 2020, ApJ, 892, 136
Tazzari, M., Beaujean F., & Testi, L. 2018, MNRAS, 476, 4527
Tazzari, M., Clarke, C. J., Testi, L., et al. 2021, MNRAS, 506, 2804
Tychoniec,Ł., Manara,C. F., Rosotti,G. P., et al. 2020, A&A, 640, A19
van der Marel, N., Birnstiel, T., Garufi, A., et al. 2021, AJ, 161, 33
Villenave, M., Benisty, M., Dent, W. R. F., et al. 2019, A&A, 624, A7
Villenave, M., Ménard, F., Dent, W. R. F., et al. 2020, A&A, 642, A164 Villenave, M., Stapelfeldt, K. R., Duchêne, G., et al. 2022, ApJ, 930, 11
White, G. J., Drabek-Maunder E., Rosolowsky, E., et al. 2015, MNRAS,
   447, 1996
Williams, J. P., & Cieza, L. A. 2011, ARA&A, 49, 67
Wolff, S. G., Duchêne, G., Stapelfeldt, K. R., et al. 2021, AJ, 161, 238
Yang, H., Li, Z.-Y., Looney, L. W., Girart, J. M., & Stephens, I. W. 2017,
            , 472, 373
Yu, T., & Chernin, L. M. 1997, ApJL, 479, L63
Zamponi, J., Maureira, M. J., Zhao, B., et al. 2021, MNRAS, 508, 2583
Zhu, Z., Zhang, S., Jiang, Y.-F., et al. 2019, ApJL, 877, L18
```